



# Mean and gravity wave structures and variability in the Mars upper atmosphere inferred from Mars Global Surveyor and Mars Odyssey aerobraking densities

David C. Fritts,<sup>1</sup> Ling Wang,<sup>1</sup> and Robert H. Tolson<sup>2</sup>

Received 5 June 2006; revised 1 August 2006; accepted 15 September 2006; published 1 December 2006.

[1] We have used density measurements obtained during aerobraking (AB) on Mars Global Surveyor and Mars Odyssey to examine mean densities and the characteristics and variability of gravity waves (GWs) in the upper atmosphere of Mars. Mean densities exhibit variability with latitude and season and in response to variable forcing and filtering from below. These data also reveal significant variability of GWs, both spatially and temporally. In general, GW amplitudes increase, while apparent horizontal scales remain the same, with increasing altitude. The dominant spatial scales at the lower AB altitudes are typically  $\sim 20$ – $200$  km and density fluctuations vary from  $\sim 5$  to  $50\%$ , though even larger values are occasionally observed. GW amplitudes also vary significantly with season, being generally larger in winter and at middle and high latitudes, and apparently reflecting mean source and filtering conditions. Amplitudes also appear to vary with longitude and time and may provide clues to variability of, and interactions with, larger-scale motions.

**Citation:** Fritts, D. C., L. Wang, and R. H. Tolson (2006), Mean and gravity wave structures and variability in the Mars upper atmosphere inferred from Mars Global Surveyor and Mars Odyssey aerobraking densities, *J. Geophys. Res.*, *111*, A12304, doi:10.1029/2006JA011897.

## 1. Introduction

[2] The Mars atmosphere appears to exhibit indications of gravity waves (GWs) and GW influences at many altitudes that parallel their characteristics and effects observed in the terrestrial atmosphere. Indeed, terrestrial observations have often provided the clues to their interpretation on Mars. Lee waves at small spatial scales and lower altitudes provided the first indications of GW influences [Briggs and Leovy, 1974; Pirraglia, 1976; Briggs *et al.*, 1979; Pettengill and Ford, 2000]. At higher altitudes, evidence for enhanced diffusion, mean temperatures far above radiative equilibrium at winter polar latitudes, and zonal jet closure provided evidence of likely GW momentum transport, possible additional turbulence transport, and a residual (meridional and vertical) circulation induced by GW instability and mean-flow interactions [Blamont and Chassefiere, 1993; Deming *et al.*, 1986; Keating *et al.*, 2002; Read and Lewis, 2004]. Finally, large ( $\sim 5$  to  $50\%$ ) fluctuations in density and/or temperature on small spatial scales ( $<10$  km vertically) in the Opportunity, Spirit, and Mars Pathfinder entry profiles, in Mars Global Surveyor (MGS) radio occultation measurements [Magalhães *et al.*, 1999; Hinson *et al.*, 1999; Creasey *et al.*, 2006], as well as small horizontal scales ( $\sim 20$  to  $200$  km)

in various Mars accelerometer data sets at aerobraking altitudes [Keating *et al.*, 1998; Tolson *et al.*, 1999, 2000, 2002; Withers, 2006] are reminiscent of similar, though smaller, fluctuations in density, temperature, wind, and atmospheric airglow intensities in the mesosphere and lower thermosphere of Earth [Fritts *et al.*, 1988, 1989, 1993, 2002]. Indeed, GW amplitudes and effects throughout the Mars atmosphere appear to be significantly larger than their terrestrial analogs in several cases (i.e., the strength of the residual circulation, departures from radiative equilibrium, and apparent GW amplitudes in the lower atmosphere and at aerobraking altitudes), suggesting that GWs may play a more dominant role in the large-scale circulation, structure, and variability on Mars than on Earth [Barnes, 1990; Theodore *et al.*, 1993; Joshi *et al.*, 1995, 1996, 1999; Collins *et al.*, 1997; Read and Lewis, 2004]. Tides and planetary waves (PWs) surely contribute to some of the observed features in the Mars atmosphere that have a primarily GW cause on Earth. However, the very large GW amplitudes inferred from descent profiles, MGS radio occultation, and accelerometer data, and apparent effects at higher altitudes, imply a very significant role for GWs in the atmospheric dynamics of Mars as well.

[3] The potentially strong influences of GWs in the Mars middle and upper atmosphere are plausible for several reasons. First, the topography on Mars is very large by analogy with Earth, with especially strong forcing expected in the tropics and at middle latitudes, where the terrain is highly structured at smaller spatial scales. More importantly, the strong winter zonal jets are believed to extend down to lower altitudes with larger amplitudes, enabling much

<sup>1</sup>Colorado Research Associates Division, NorthWest Research Associates, Boulder, Colorado, USA.

<sup>2</sup>College of Physical and Mathematical Sciences, North Carolina State University, Raleigh, North Carolina, USA.

stronger GWs arising from topography than on Earth. The zonal jet structures are expected to continue to increase with altitude up to  $\sim 60$  km or above under fall, winter, and spring conditions [Banfield et al., 2003; Read and Lewis, 2004], unlike Earth, where zonal wind minima constrain mountain wave amplitudes in the lower stratosphere of each hemisphere. Zonal jets are also expected to achieve significantly larger maximum mean winds than on Earth ( $\sim 2$  times larger). These larger mean winds potentially permit significantly larger GW amplitudes, larger vertical wavelengths and group velocities, and larger energy and momentum fluxes extending to higher altitudes than in Earth's middle atmosphere [Barnes, 1990; Joshi et al., 1995; Collins et al., 1997]. Indeed, several authors have found that inclusion of GW effects, either directly or via parameterization, improves the performance of their models at lower and higher altitudes [Barnes, 1990; Collins et al., 1997; Forget et al., 1999; Rafkin et al., 2001; Angelats i Coll et al., 2005]. Others have inferred their likely role due to differences between observations and model results that do not include these effects at present [Bougher et al., 2006a]. These various studies imply both large GW influences and variability in the Mars atmosphere and a potential to begin to quantify these effects directly through detailed analyses of accelerometer data because of their large density perturbations. Such GW effects may also be included indirectly through various assimilation methods, which are intended to constrain the numerical solutions of Mars General Circulation Models (GCMs) by observations as fully as possible and which therefore include the effects of GW energy and momentum transports based on the data being employed [Banfield et al., 1995; Lewis and Read, 1995; Lewis et al., 1996, 1997; Houben, 1999; Zhang et al., 2001].

[4] While topography is perhaps the most obvious source of large GWs in the Mars atmosphere, it is surely not the only source. Strong wind shears, convection, wave-wave interactions, and local body forces are known to be significant on Earth and surely are also operative on Mars (see Fritts and Alexander [2003] for a terrestrial review). Indeed, Creasey et al. [2006] found little correlation of inferred GW potential energies at lower altitudes with underlying topography, though it is not certain whether this indicates additional GW sources, strong filtering effects, satellite measurement biases, as are known to occur on Earth [Jiang et al., 2004], or a combination of effects. We have learned, however, that linear descriptions of GW dynamics, while not complete, offer many valuable insights and are useful in the interpretation of observations in many cases, despite their simplicity. Examples in the terrestrial atmosphere include approximately linear GW responses to strong convection at the Earth's mesopause [Taylor and Hapgood, 1988; Sentman et al., 2003], ray tracing of observed GWs to apparent local or remote sources [Guest et al., 2000; Hertzog et al., 2002; Preusse et al., 2002], linear analyses of large-amplitude GWs leading to instability and turbulence [Yamada et al., 2001; Fritts et al., 2002], and predictions of GW amplitudes and influences under a variety of forcing and filtering conditions [Marks and Eckermann, 1995; Eckermann and Marks, 1997; Vadas and Fritts, 2004, 2005, 2006]. Indeed, the linear GROGRAT ray-tracing model that has been employed successfully

in a number of terrestrial applications has been modified for the Mars atmosphere [Joshi et al., 1999] to describe the temperature structures observed during the Mars Pathfinder descent [Magalhães et al., 1999]. Terrestrial studies have confirmed that even in the presence of multiple GW sources, mountain waves (MWs) dominate GW variances at greater altitudes over high terrain and under strong surface wind and suitable propagation conditions [Jasperson et al., 1990; Nastrom and Fritts, 1992; Jiang et al., 2002, 2003]. The messages from these studies are (1) that MWs on Mars likely account for a significant fraction of the GWs present throughout the Mars atmosphere over high and variable terrain, (2) other sources and filtering are likely to contribute to definition of the GW spectrum, and (3) that linear theory applied to such waves should yield similar insights and an increased understanding of their various atmospheric effects.

[5] Given the importance of understanding the Mars atmospheric circulation, structure, and variability, and the likely importance of GWs in these dynamics, we are performing analyses employing accelerometer measurements of densities obtained during MGS and Mars Odyssey (ODY) aerobraking. We are using these data to quantify both mean densities, temperatures, and scale heights and GW amplitudes, their spatial (altitude, latitude, and longitude) and temporal (seasonal and short term) variations, the inferred perturbation temperatures and winds, and their potential influences on the circulation and structure of the Mars upper atmosphere. Our purpose here is to provide the initial results of this analysis.

[6] Our paper is organized as follows. Section 2 describes the spatial and temporal coverage of MGS and ODY data, an overview of the mean densities and other inferred fields, and an assessment of measurement uncertainties with altitude and time. GW amplitudes, variances, and spectra, and their spatial and temporal variability, are described in section 3. Section 4 includes a discussion of these results and of their possible implications. Our summary and conclusions are provided in section 5.

## 2. MGS and ODY Analysis and Mean Fields

### 2.1. MGS Data

[7] MGS began aerobraking at Mars in September 1997 and ended in February 1999 on orbit 1283 with the orbital period below 2 hours. There were two interruptions in aerobraking during the mission: the first from orbit 19 to orbit 40 due to a broken solar array, and a second, 6-month aerobraking hiatus occurring from orbit 202 to 573. The broken solar array led to occurrences of  $\sim 7$ -s oscillations of the spacecraft accompanying differential drag or thrust maneuvers that impact sensitivity to small-scale ( $\sim 30$  km and less) density variations. However, these oscillations appear not to have influenced measurements of mean and larger-scale motions. Throughout the mission, the inclination was  $\sim 93^\circ$ , MGS sensitivity was between 0.6 and 1 kg/km<sup>3</sup> for a 1-s integration, and mean density at periapsis was  $\sim 20$  kg/km<sup>3</sup>. MGS provided sensitivity to all latitudes south of  $60^\circ\text{N}$  and to primarily fall and winter conditions in both hemispheres, and periapsis on MGS dipped as low as  $\sim 100$  km within the south polar winter vortex (see Figure 1).

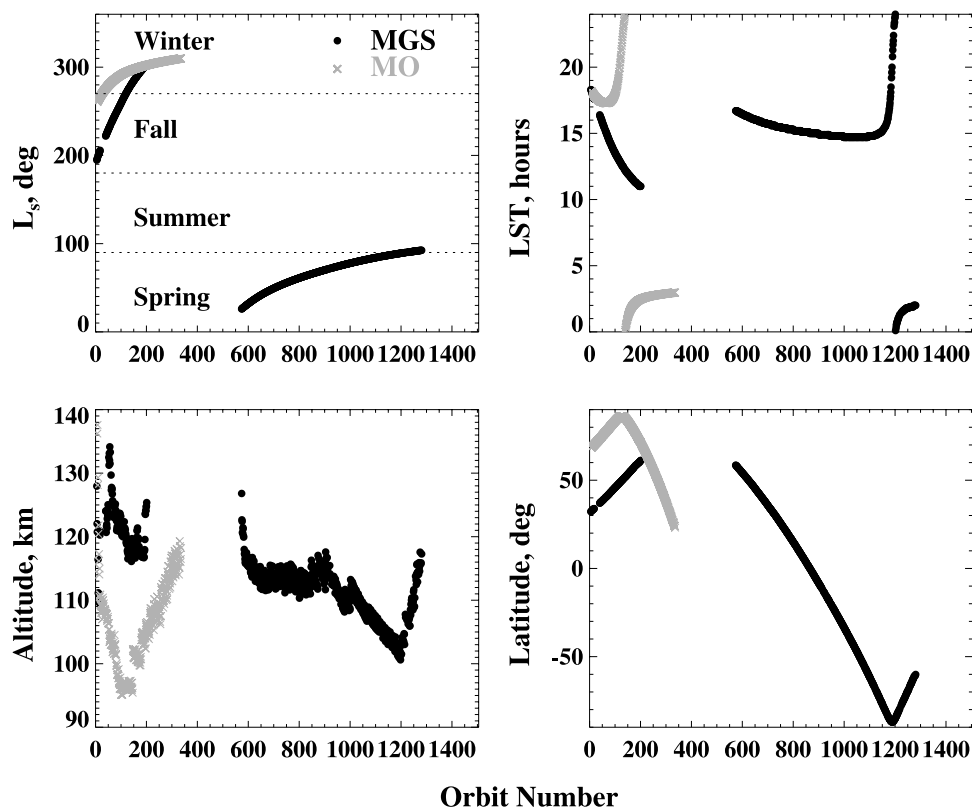


**Figure 1.** Celestial longitude (top left), local solar time (top right), altitude (bottom left), and latitude (bottom right) of periapsis during Mars Global Surveyor (MGS) (blue) and Mars Odyssey (ODY) (red) aerobraking. Aerobraking on MGS ceased from orbit 202 to 573 to compensate for earlier damage to the solar array. Note that MGS provided sensitivity to fall and winter conditions in each hemisphere, while ODY sampled primarily northern hemisphere winter conditions [after Tolson *et al.*, 2002].

[8] A seven-orbit mean of density variability during MGS aerobraking as a function of latitude is shown in the upper panel of Figure 2. As seen in the lower left panel of Figure 1, periapsis altitude variability was small, except near the South Pole, so the density variability at middle and lower latitudes likely reflects perturbations due to various atmospheric motions. In particular, note that maximum variability appears to correlate with the positions of the mean zonal jets under either equinox or winter conditions, suggesting that our hypothesis that strong zonal winds allow large-amplitude GWs to penetrate to high altitudes may be reasonable. The weaker variability at tropical latitudes likewise seems to agree with an expectation of smaller GW excitation and amplitudes where mean winds are weaker. Note, however, that MGS data were not used to examine GW fluctuations because a 7-s average was applied to remove the effects of the solar array oscillations.

[9] Despite the lack of sensitivity to small-scale fluctuations during MGS aerobraking, MGS density data were found to be valuable in defining the mean structure of the lower thermosphere during Mars fall, winter, and spring [Bougher *et al.*, 2006b; Withers, 2006]. The latitude coverage during spring was by far the greatest, and the inferred mean density, stability ( $N^2$ ), density scale height, and “pseudo” temperature inferred from the density scale height are shown as functions of latitude and altitude in Figure 3.

[10] Several interesting atmospheric phenomena occurred during the MGS mission and influenced these density measurements. The regional Noachis dust storm in the southern hemisphere occurred around orbit 50 causing the nominal thermospheric density near  $\sim 115$ – $135$  km to more than double in a few days at northern middle latitudes [Keating *et al.*, 1998; Bougher *et al.*, 2006a, also see Figure 4]. This was followed by a relaxation back to the nominal atmospheric structure over  $\sim 50$  to 100 days [Keating *et al.*, 1998]. Also present during a majority of these aerobraking passes were small-scale, large-amplitude density perturbations that we believe to be the signatures of GWs, and we will employ the ODY data to examine these in greater detail below.

## 2.2. ODY Data

[11] ODY began aerobraking in October 2001 and ended 325 orbits later in January 2002. ODY also had an orbital inclination of  $\sim 93^\circ$ , and no mission anomalies affected the spatial data coverage. The sampling rate was reduced twice during the mission, on orbits  $\sim 135$  and 270, resulting in the higher noise levels noted in Figure 2 above [Tolson *et al.*, 2002]. The mean structures displayed above for MGS data in spring, but inferred from ODY data during winter, are shown in Figure 5. Note the temperature increase approaching the pole, rather than the decrease expected before these measurements were made [Keating *et al.*, 2002; Bougher *et*

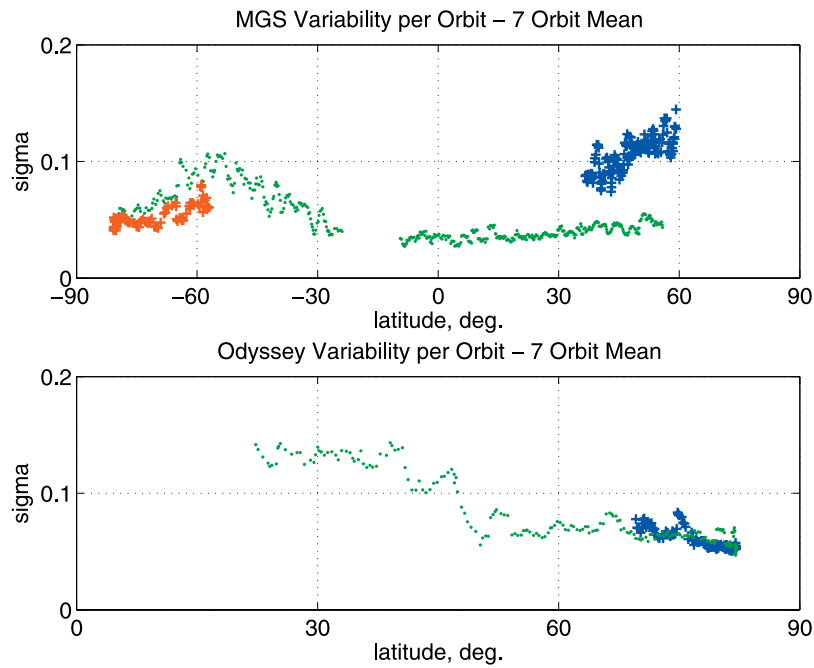


**Figure 2.** Seven-orbit density variability during aerobraking by MGS (top) and ODY (bottom). Blue crosses (top) were during orbits 40–201 when MGS was near the winter pole and during a dust storm. Green dots (top) show phase 2 (starting 6 months later) extending into SH winter. Red crosses (top, after passing the pole) show comparable daytime and nighttime variability. For ODY, the blue crosses are the earlier orbits with periaapsis precessing toward the pole. Initial high ODY variances near 70°N are real, but high variability south of ~60°N is due to increases in noise level after orbits ~135 and 270 [after Tolson *et al.*, 2002].

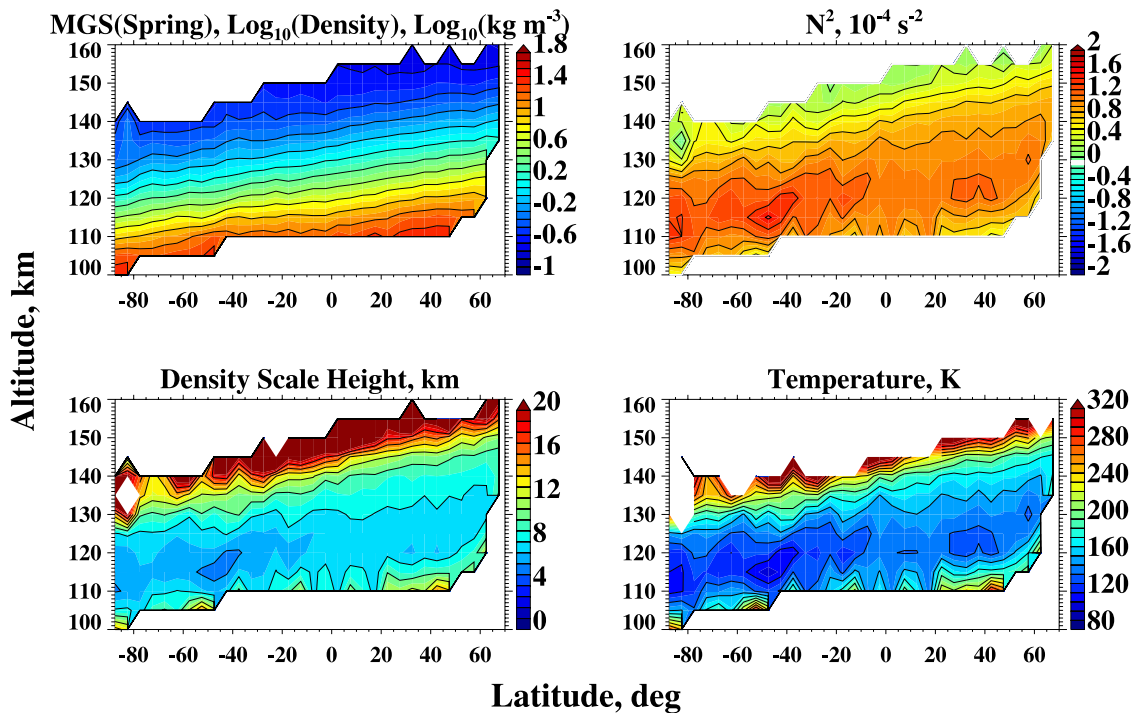


**Figure 3.** Mean density, stability ( $N^2$ ), density scale height, and “pseudo” temperature (inferred from the density scale height) as functions of latitude and altitude inferred from MGS aerobraking density measurements. Fall and winter data reveal opposite slopes of these fields at high northern latitudes (see Figure 5).

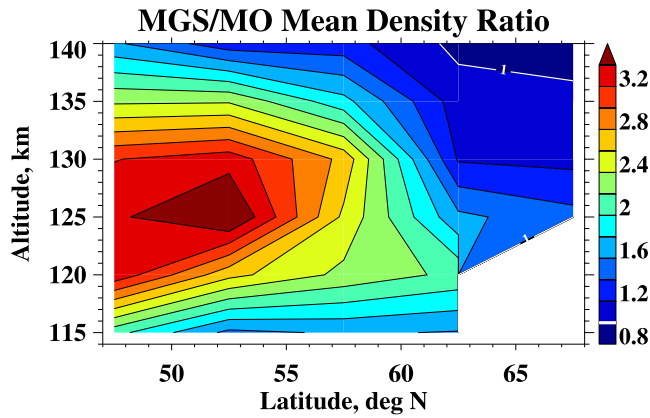


**Figure 4.** Ratio of mean density during the Noachis dust storm during the MGS mission relative to that at the same latitude and season measured during ODY, but without an active dust storm. Note that thermospheric densities increased by a factor of  $\sim 2$ – $3.6$  over altitudes of  $\sim 115$ – $135$  km at northern middle latitudes, but also that these data were obtained at a different local time than those shown in Figure 3.

*al.*, 2006a]. This tendency is even more pronounced if we plot only data from the initial orbits  $\sim 7$ – $134$  (not shown), but those data are much more restricted in latitude (see Figure 1).

[12] In order to evaluate what ODY data are suitable for estimates of GW parameters, we computed histograms of 1-s density estimates in 5-km altitude intervals for each of the three phases of ODY data collection: orbits  $\sim 7$ – $134$

(up to day  $\sim 42$ , with low noise); orbits  $\sim 135$ – $269$  (with intermediate noise); and orbits  $\sim 270$  and after (with high noise). These data are shown together in Figure 6. Note that later data extend only down to  $\sim 110$  km because periastron altitude increased sharply in the final stages of ODY aerobraking (Figure 1). At altitudes of 120 km and below, essentially all of the density estimates are positive and the three different noise levels yield similar distributions because densities are relatively large and S/N is high. At increasing altitudes, however, the later (higher-noise) data exhibit increasing numbers of negative density estimates until, at  $\sim 140$  km and above, the histograms have broad distributions seemingly centered near zero. In contrast, the earlier, low-noise density data have a negligible fraction of negative estimates to altitudes approaching  $\sim 140$  km. The result is expected to be confidence in inferred GW perturbation density variances from  $\sim 95$ – $140$  km for orbits 7–134, from  $\sim 95$ – $125$  km for orbits 135–269, and from only  $\sim 110$ – $120$  km for orbits 270 and after.

[13] The implications of these uncertainties in density estimates are explored by computing the mean densities obtained by averaging over the distributions shown in Figure 6. These means were computed by averaging both over all density estimates, positive and negative, and over only the positive density estimates, and the results are displayed in the upper panel of Figure 7. At lower altitudes, where densities and S/N are large, all orbits yield similar results. Where higher noise levels and smaller densities contribute increasing numbers of negative density estimates; however, the averages over only positive density estimates depart sharply from those using all density data and are clearly wrong. However, there are also apparently systematic biases in the means obtained by averaging over all

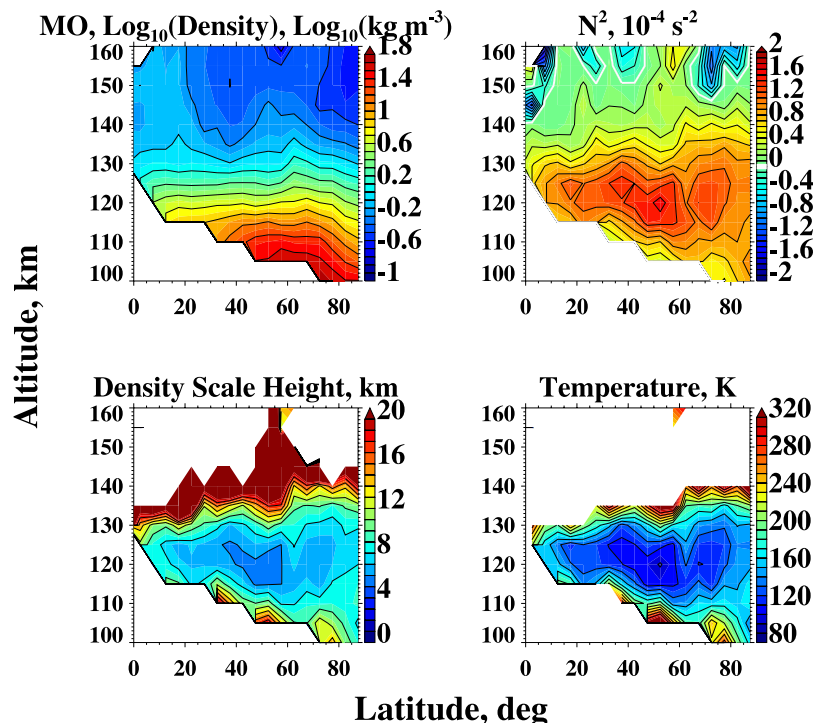


**Figure 5.** As in Figure 3, but for ODY during northern hemisphere winter.

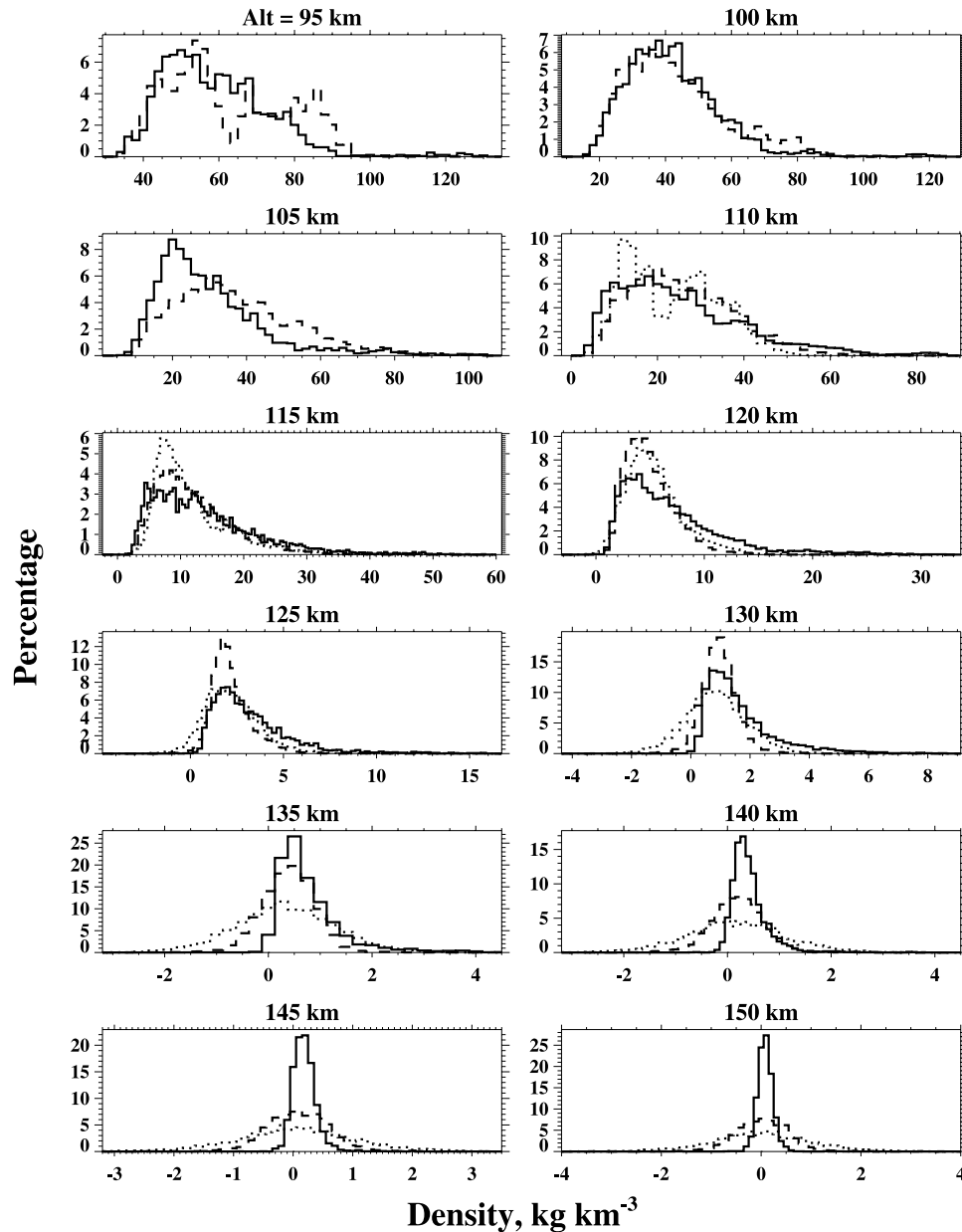


**Figure 6.** Histograms of 1-s densities in 5-km altitude bins during the three phases of ODY measurements. Solid values are for orbits 7–134, dashed values are for orbits 135–269, and dotted values are for orbits 270 and after. Dotted distributions are missing at the lowest altitudes, as periaresis occurred at altitudes of  $\sim 110$  km and above for these later orbits (see Figure 1). Note that all density estimates are positive where densities are large, accelerometer sampling is faster, and noise is lower. At later times, however (the dashed and dotted distributions), and especially at the higher altitudes where densities are smaller, increasing fractions of 1-s density estimates are negative. Indeed, late estimates (dotted) at and above 140 km seem nearly centered on zero.

density values, as the higher-noise mean values (with broader distributions and more negative values) decay more rapidly with altitude than the lower-noise, earlier data. While it is possible that these differences, because they are separated in time, represent a real variation in the mean density profile with time, we choose to be more conservative and assume that we can only trust the earlier data yielding the higher mean densities at the highest altitudes.

These data suggest that mean values are valid to  $\sim 160$  km or higher for orbits 7–134, and that variances are likely reasonable to  $\sim 140$  km for these data. However, as noted earlier in connection with Figure 6, we should be wary of density variances employing the higher-noise data above  $\sim 120$ – $125$  km. Thus we will employ only the earlier, lowest-noise data for all of our GW studies below. The vertical variations of density scale height accompanying

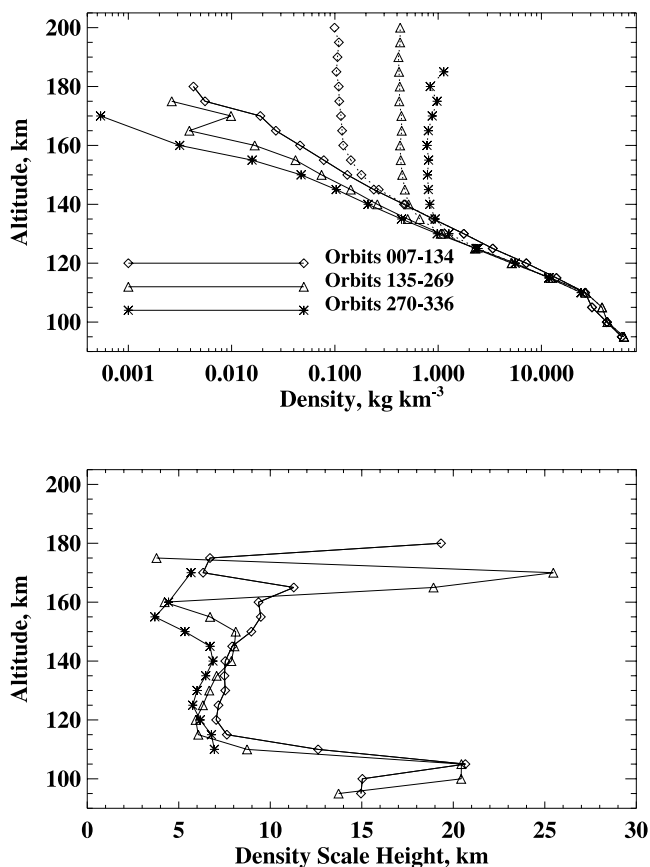


**Figure 7.** Mean densities (top) and density scale heights (bottom) based on the ODY data summarized in Figure 6. As above, these are for density estimates before (diamonds), after one (triangles), and after a second (asterisks),  $2\times$  decimations in accelerometer sampling, as described in Figures 2 and 6. Estimates are based on all (solid) and only positive (dotted) 1-sec density estimates at each altitude and mission phase. These data suggest biased mean densities and scale heights at higher altitudes and later times where S/N is lower, whether negative density estimates are included or excluded.

these mean density estimates are shown in the lower panel of Figure 7. These show clearly the more rapid decay of mean density with altitude implied by the higher-noise data.

### 3. Inferred Gravity Wave Amplitudes and Variances

[14] Density estimates observed near periapsis on six selected orbits during the early and middle phases of aerobraking are shown in Figure 8 and exhibit the large apparent GW density perturbations ( $\sim 5\text{--}50\%$ ) and small spatial scales ( $\sim 20\text{--}200$  km) noted above. Indeed, the 39-s running means are seen in four of these six profiles (orbits 7, 12, 115, and 215) to track the lower-frequency features. Thus they significantly underestimate wave amplitudes at spatial scales of  $\sim 200$  km and longer. Corresponding fractional density perturbations relative to 39-s running

means are shown in Figure 9. At higher altitudes ( $|t| > \sim 200$  s), uncertainties are too large for ODY (and MGS) data to allow useful determinations of fluctuations at small scales, and we have elected to show data only at the lower altitudes where we have greater confidence. As noted above, the dominant spatial scales seen in these data are a few to  $\sim 50$  s, or  $\sim 20\text{--}200$  km at an average orbital velocity of  $\sim 4$  km  $s^{-1}$ , similar in scale and amplitude to those noted by *Withers* [2006]. Note that fluctuations appear to exhibit significant spatial coherence, even at the highest altitudes, where densities are  $\sim 1$  kg  $km^{-3}$  or less. Clearly, we are approaching the noise limits at these sites, but there is nevertheless some coherence at smaller scales (see the  $\sim 5$  to 15-s, or  $\sim 20$  to 60-km, fluctuations at the highest altitudes of orbit 7 and the descending portions of orbits 108 and 115). The character of these structures is explored further below.

[15] Fractional density perturbations were used to assess the inferred GW variances with longitude and altitude, and the results of this analysis are displayed in Figure 10. Note, in particular, that the variance enhancements between  $\sim 130$  and  $180^\circ$  longitude, and to a lesser extent between  $\sim 0$  and  $50^\circ$  longitude, exhibit significant coherence in altitude. However, these data arise from only a few ( $\sim 20$ ) orbits, from orbits  $\sim 40$  to 60, and may thus reflect a temporal rather than a spatial variability of inferred GW variances. There is, nevertheless, a correlation of these variance maxima with maxima of local mean densities suggestive of nonmigrating tidal and/or planetary-wave signatures noted in MGS and ODY data [*Banfield et al.*, 2000; *Forbes and Hagan*, 2000; *Keating et al.*, 2001; *Wilson*, 2002; *Wang et al.*, 2006]. This could result from filtering of the GW field by the nonmigrating tidal structures, but this correlation will be explored further in that follow-up paper.

[16] To examine the temporal variation in GW variances, we display variations of GW fractional density variances in time and in 5-km altitude bins in Figure 11. While there is significant orbit-to-orbit variability in orbital variance (likely due both to temporal variability of the GW field and to estimates of variances based on limited sampling within each altitude bin), there are also apparent periodicities as well. We note variance variations having periods of  $\sim 3$  to 5 days and having coherence over altitudes from 110 to 125 km from day  $\sim 10$  to 25. This may provide evidence of spatial variations, and possible sensitivity to source or filtering conditions, with further analysis. However, we judge the data to be too limited at this stage of aerobraking to have confidence in such results without additional study. At later stages in aerobraking, the orbital period becomes significantly smaller and sampling is more frequent, but the coherence in altitude and in time also appears to shift to longer periods.

[17] We explore this further by applying a 5-day running mean to these variances. The results are shown with the heavy lines in Figure 11 and jointly for the lowest six altitudes in Figure 12. Despite the smoothing, there remain traces of the short-term variability at early times noted above, as well as at later times and higher altitudes. Additionally, these running means exhibit clear lower-frequency variations in GW variances (with periods of  $\sim 10$  to 20 days), as well as clear correlations of these

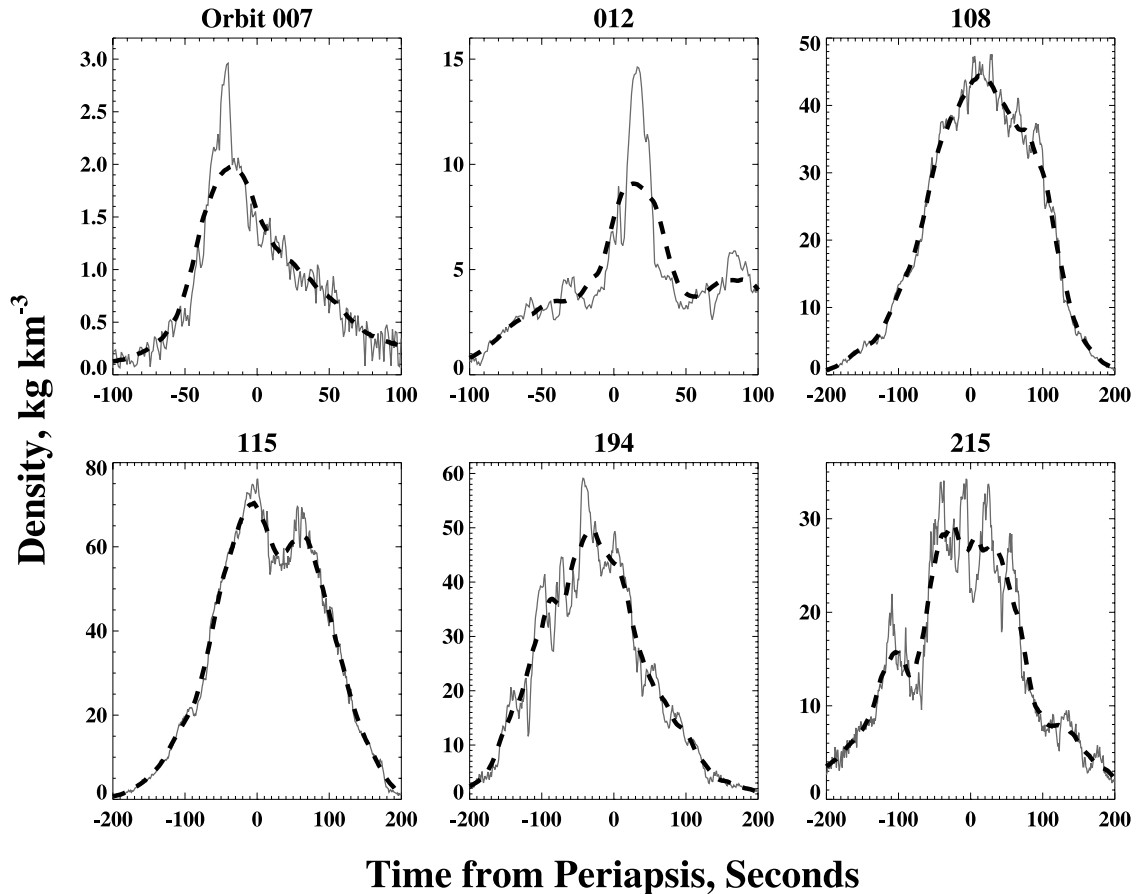


**Figure 8.** Density estimates at 1-s intervals for selected orbits during the early (low-noise) and middle (medium-noise) phases of ODY aerobraking. Shown are the raw 1-s density estimates (thin-solid) and the 39-s running means (bold-dashed) which we have employed to evaluate local density perturbations attributed to gravity waves (GWs). Note that in most cases, the 39-s running mean likely represents the real mean fairly well. There are orbits, however, for which this is not optimal, and where underestimates of density perturbations are a result. Orbits 12 and 115 are examples of orbits for which this procedure leads to an underestimate of the amplitudes of apparent motions having longer periods that are not adequately captured by this procedure. Note also the smaller intervals shown for the earlier two orbits having periapsis at higher altitudes.

variations in GW variances between adjacent, and independent, altitudes (see Figure 12). We note, in particular, the following features: (1) the largest variances occur at the highest altitudes at the earliest times; (2) variances increase with time at all altitudes prior to day  $\sim 44$  (but with variations that occasionally exhibit vertical coherence, i.e. see the relative peaks at days  $\sim 21, 28, 37,$  and  $44$ ); (3) variances decrease strongly at all altitudes after day  $\sim 45$  (but beginning first at the highest altitudes); and (4) a second variance peak occurs at day  $\sim 60$ , but exhibits the greatest relative maxima at altitudes of  $\sim 120$  km and below.

[18] Finally, we compute spatial spectra of the fractional density perturbations for data segments about periapsis that are sufficiently short to provide sensitivity to possible changes in GW propagation, and spectral shape, with altitude. Mean spectra in each of four periapsis altitude ranges (95–100, 100–105, 105–110, and 110–130 km) are

shown in Figure 14. These results are discussed further below.

#### 4. Discussion

[19] Given that all of the ODY measurements occurred at high latitudes in northern hemisphere winter, we expect that seasonal and latitudinal variations in GW source or filtering conditions likely did not contribute to the temporal variations of GW variances seen in Figures 11 to 13. According to the various Mars GCMs that have been developed to date, we expect a zonal (eastward) jet with wind speeds exceeding  $\sim 140 \text{ ms}^{-1}$  extending from  $\sim 60$  to  $75^\circ$  in latitude and from  $\sim 30$  to  $80$  km in altitude, with lower (eastward) wind extending from  $\sim 30^\circ$  to the pole and from the surface to above  $120$  km [Read and Lewis, 2003]. Thus all of these measurements should have occurred at the upper levels of the winter zonal jet. The observed periodicities are comparable to various PWs of the Mars lower atmosphere,

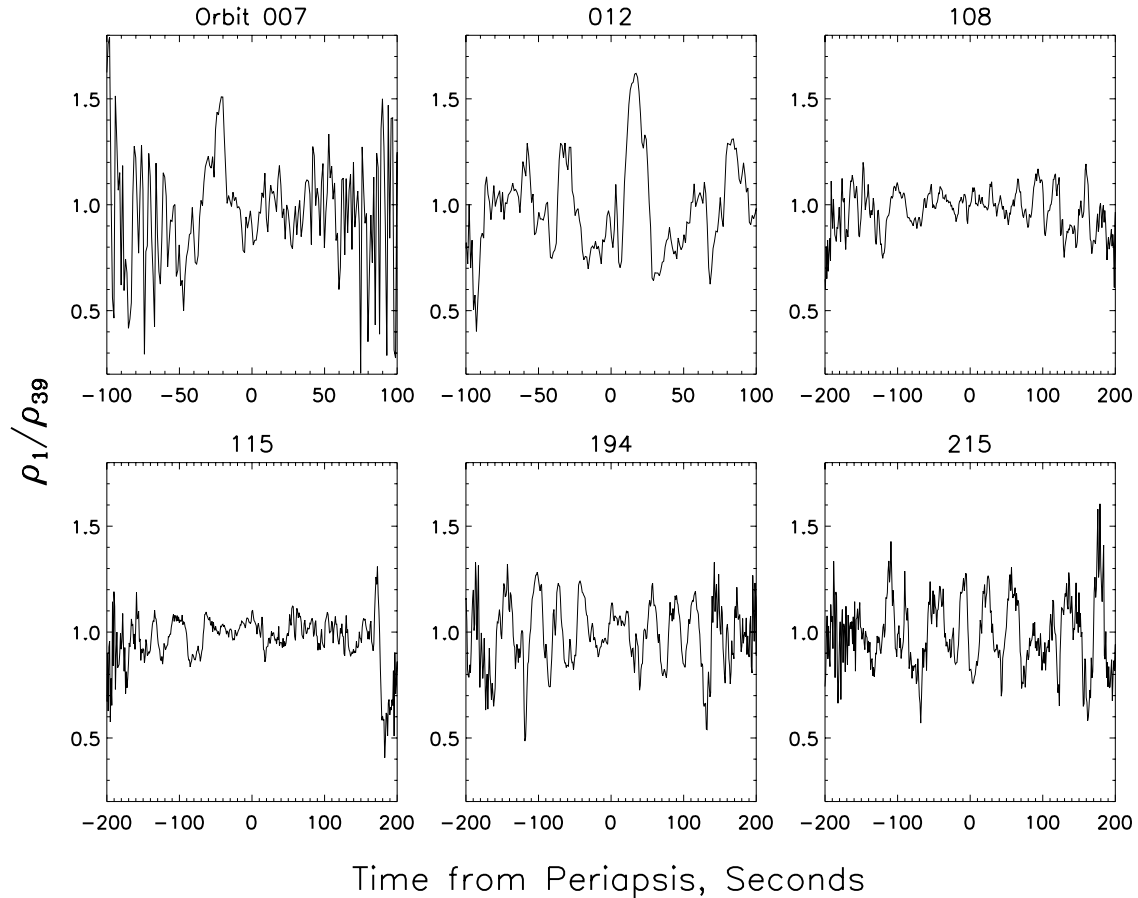


**Figure 9.** Density ratios (ratios of 1-s to 39-s running mean densities) obtained for the ODY orbits shown in Figure 8 at altitudes of  $\sim 100$  to  $130$  km. In each case, time zero corresponds approximately to periapsis. At a velocity of  $\sim 4$  km/s, these fluctuations correspond to horizontal scales of  $\sim 10$ – $100$  km. Density perturbations assumed due to GWs are occasionally as large as  $\sim 60\%$ . Note, in particular, that the  $\sim 60$ -s,  $\sim 200$ -km, variations seen in orbits 12 and 115 in Figure 8 are not represented well in these perturbation estimates.

suggesting a possible sensitivity of the aerobraking data to longitudinal variations following those seen in Figure 10. To explore this further, we have attempted various sampling and partitioning schemes but found none that provides a clear indication of preferential longitudinal filtering beyond what was seen in Figure 10. If filtering was the cause, the varying profiles with time suggest suppression of vertical propagation at earlier times and at the lowest altitudes, larger zonal winds extending to higher altitudes allowing larger variances throughout these altitudes for days  $\sim 20$  to  $45$ , and descents of (westward) zonal wind shears unfavorable to GW penetration to higher altitudes beginning day  $\sim 45$  and at lower altitudes at day  $\sim 60$  (see Figure 13).

[20] While this is only speculation without supporting data on the large-scale wind fields, the variability of GW variances noted above suggests possible modulation by (1) variable GW sources at lower altitudes, (2) filtering by intervening winds, or more likely (3) a combination of the two processes. Variable sources are suggested by the variations of surface flows and wind shears likely to accompany traveling PWs, which exhibit time scales spanning the range of variability noted in Figures 11 and 12,  $\sim 3$  to  $20$  days [Banfield *et al.*, 2004]. Variable filtering environments would accompany both these PWs at lower altitudes and

the larger migrating and non-migrating tides at higher altitudes. Indeed, the longitude band of our observed GW variance enhancement corresponds closely to longitudes exhibiting the maximum zonal densities [Wang *et al.*, 2006] accompanying the major eastward nonmigrating diurnal tide, or Kelvin wave [Wilson and Hamilton, 1996; Forbes and Hagan, 2000], suggesting a potential link between enhanced GW variances and the large-scale wave structures accounting for the density maxima at these same locations. The small GW variances suggested by MGS data at lower latitudes (upper panel of Figure 2), but not evaluated in detail here, are likewise expected to result from filtering by weak westward winds at higher altitudes which both block MW penetration and limit intrinsic phase speeds and amplitudes of those GWs excited by other sources.

[21] The spatial spectra shown in Figure 14 are believed to represent essentially horizontal spectra of density fluctuations for reasons articulated previously by Fritts *et al.* [1989, 1993]. Essentially, density perturbations are related to horizontal wind perturbations through the relation

$$\rho' / \rho_0 \sim (N/g)u'_h, \quad (1)$$

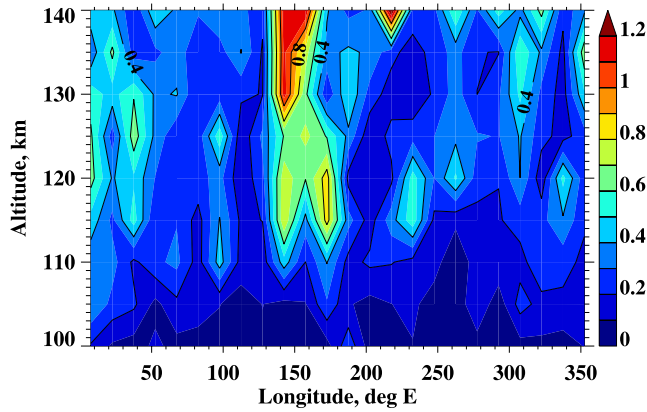


**Figure 10.** ODY winter hemisphere density variances scaled by mean density in  $15^\circ$  and 5-km bins as functions of longitude for orbits 7-134. The most significant values occur at longitudes of  $\sim 130$ – $180^\circ$ . Large variances are a result of the high skewness of the density estimates seen in the solid-line distributions at altitudes of 140 km and below in Figure 6. Variance growth is slower than  $\rho^{-1}$  with altitude, suggesting significant GW dissipation, turbulent mixing, and energy and momentum flux convergence at these altitudes.

where  $\rho_0$  is mean density,  $N$  is the buoyancy frequency,  $g$  is gravity, and primes denote perturbation quantities [also see *Fritts and Alexander, 2003*]. This is because density and wind perturbations are strongly constrained by saturation criteria that place limits on GW wind shears of  $du'_h/dz \sim N$ , which severely restricts  $u'_h$  (thus also  $\rho'$ ) when vertical scales are small.

[22] The spatial spectra exhibit slopes close to  $-2$ , which is a typical value for horizontal wind and temperature fluctuation spectra seen in the atmosphere of Earth. These spectra also exhibit a growth in amplitude by a factor of  $\sim 5$  over these altitudes, suggesting (as on Earth) that the GW field is undergoing strong dissipation, likely due to nonlinear instability and wave-wave interaction dynamics, throughout this altitude range. In the absence of such processes, we would anticipate that spectral amplitudes would increase as  $\rho^{-1}$  with increasing altitude, and the observed growth is much less than we would expect over multiple scale heights for conservative GW propagation. We also note that there is no appreciable change in the spectral slope with altitude. Together, these results suggest (1) that these observations are at altitudes where nonlinear dynamics (and instability processes) are dictating GW amplitudes and spectral character, (2) that the turbopause on Mars is therefore at a greater altitude in winter (hence a much greater depth over which strong turbulent transport occurs, relative to Earth), and (3) that the GW spectrum dictated by viscous dissipation of GW motions must not occur until even greater altitudes. The apparent occurrence of strong GW instability and saturation at these altitudes provides further support for the possible influences of mean wind shears and their constraints on GW variances with altitude discussed in connection with Figures 11 to 13 above. We note, however, that it is likely not reasonable to assume that these GWs are propagating zonally, nor that they arise only

from topography, as topography can excite GWs having a range of propagation directions and there are surely other GW source mechanisms that are also at work in the Mars atmosphere, as on Earth. Indeed, the spatial scales suggested by the spectra in Figure 14 are the projections of the GW structures along the aerobraking orbit and are therefore generally larger than along the direction of propagation of the GW.

[23] Finally, it is of interest to ask how large the GW momentum fluxes might be at these altitudes, given what we know, and can infer, of apparent GW amplitudes and spatial scales. The horizontal and vertical perturbation velocities ( $u'_h$ ,  $w'$ ) within a midfrequency GW (neglecting rotation, scale height, and nonhydrostatic effects [*Fritts and Alexander, 2003*]) are related to the horizontal and vertical wave numbers ( $k_h$ ,  $m$ ), or alternatively the buoyancy and intrinsic GW frequencies, through the continuity equation as

$$w' = -ku'_h/m = -\omega u'_h/N, \quad (2)$$

where  $\omega$  is the GW intrinsic frequency. We can also estimate the maximum horizontal perturbation velocity and the maximum horizontal wavelength of a representative GW from the density amplitudes and apparent horizontal scales seen in Figures 8 and 9 above. We will take fractional density perturbations and apparent horizontal wavelengths of  $\sim 20\%$  and 100 km as representative, though smaller spatial scales and larger amplitudes are also prevalent, and will have significant implications for inferred momentum fluxes as well (see below). We will also take  $N \sim 10^{-2} \text{ s}^{-1}$  as representative of altitudes near  $\sim 100$  km. Finally, we can estimate a likely minimum vertical wavelength (thus maximum  $m$ ) based on the fractional density perturbation,  $u'_h \sim N/m$ , from the saturation constraint above. With these approximate relations, the GW momentum flux (per unit mass) averaged over the GW phase may be written as

$$\langle u'_h w' \rangle = -(k_h/2m)u_h'^2 = (k_h/2N)u_h'^3 \sim (k_h g^3/2N^4)(\rho'/\rho_0)^3. \quad (3)$$

Thus the most important GWs in the Mars middle and upper atmosphere, in terms of the transport of momentum and the potential for strong wave-wave and wave-mean flow interactions, are those that have large fractional density perturbations and small horizontal scales (large  $k_h$ ), and which are also the easiest GWs to measure. Note, however, that these are not the GWs that are observed in limb measurements, such as those observed by *Creasey et al. [2006]*, as limb measurements are biased toward larger horizontal scales, typically  $\sim 200$ – $400$  km or larger, and which, due to the dependence of equation (3) on  $k_h$ , likely do not contribute as much to transport, forcing of larger-scale motions, and turbulence (because energy and momentum fluxes scale in similar ways with GW parameters) as GWs at smaller horizontal scales [see *Fritts and Alexander, 2003*].

[24] With equations (1)–(3), we can estimate typical values of  $u'_h$ ,  $w'$ , and GW momentum fluxes at altitudes near  $\sim 100$  km on Mars. Note that smaller real GW horizontal wavelengths (along the GW propagation direction) and/or larger vertical wavelengths than estimated from

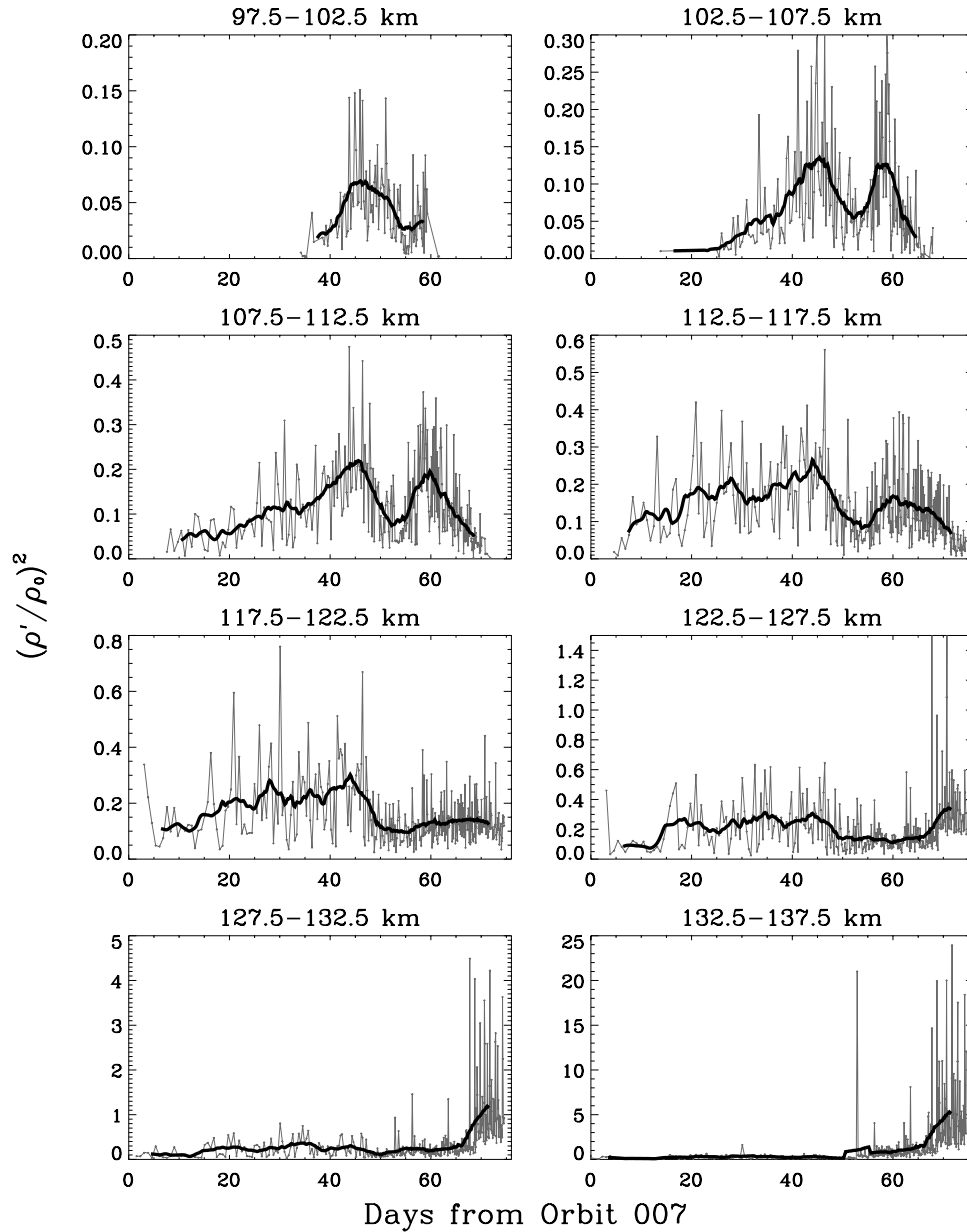


**Figure 11.** ODY winter hemisphere fractional density variances scaled by mean density in 5-km bins as functions of time from orbit 7. The bold-solid lines are 5-day running means for each altitude bin. Note the strong temporal variability on time scales of  $\sim 10$ – $20$  days and the strong correlations between adjacent altitude bins. Orbits 135 and 270 occurred on days 52 and 69, so the large variances at altitudes of 125 km and above at later times are a result of the decimation in accelerometer sampling discussed in connection with Figure 6.

the observed spatial scales and fractional density amplitudes would only increase the estimate of  $w'$  relative to  $u'_h$ , thus also increasing the estimate of momentum flux. Larger fractional density perturbations likewise imply larger momentum flux estimates according to equation (3). For the values chosen as representative, we obtain typical horizontal and vertical velocity perturbations of  $u'_h \sim 70 \text{ m s}^{-1}$  and  $w' \sim 60 \text{ m s}^{-1}$  and a typical momentum flux of  $\sim 2000 \text{ m}^2 \text{ s}^{-2}$ . Clearly, the occasional much larger fractional density perturbations, or much smaller horizontal scales having comparable GW amplitudes, would yield

correspondingly larger velocity and momentum flux estimates.

[25] For reference, by far the largest estimate based on measurements at similar altitudes in Earth's middle atmosphere is  $\sim 900 \text{ m}^2 \text{ s}^{-2}$  by *Fritts et al.* [2002], with more typical “large” values of  $\sim 50$ – $100 \text{ m}^2 \text{ s}^{-2}$  and mean values another order of magnitude smaller. Nevertheless, the estimates on Mars are plausible for a number of reasons. First, fractional density amplitudes on Mars are far larger, in general, than comparable amplitudes at similar altitudes and mean densities on Earth [*Fritts et al.*, 1989, 1993]. Second, Mars GW forcing is arguably much stronger than

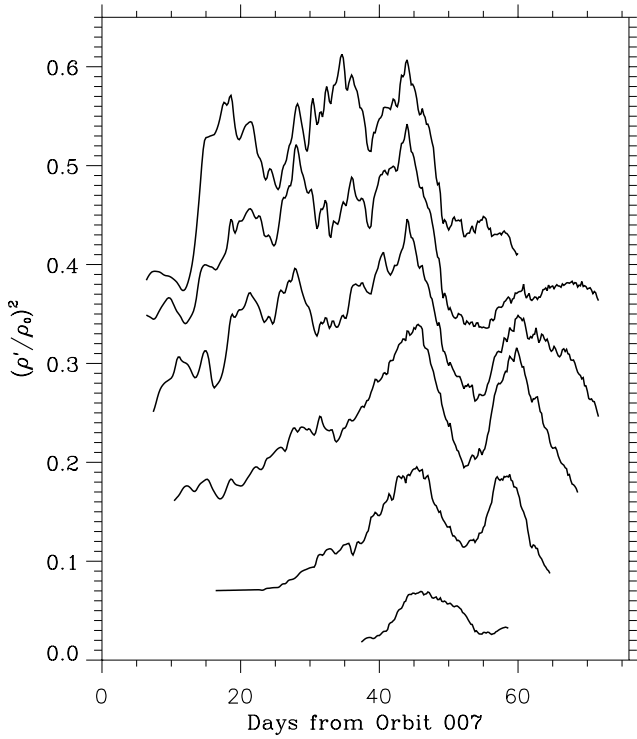


**Figure 12.** As in Figure 11, but showing the 5-day running-mean variances together, with the variances at successively higher altitudes displaced by 0.06 units. Note the high coherence between altitudes at timescales of  $\sim 10$ – $20$  days, with the relative maximum centered at day  $\sim 45$  extending from  $\sim 95$ – $130$  km, but the later maximum at day  $\sim 60$  extending only from  $\sim 95$ – $115$  km. Such large correlation depths are to be expected for GWs that have large fractional density perturbations (see text for details).

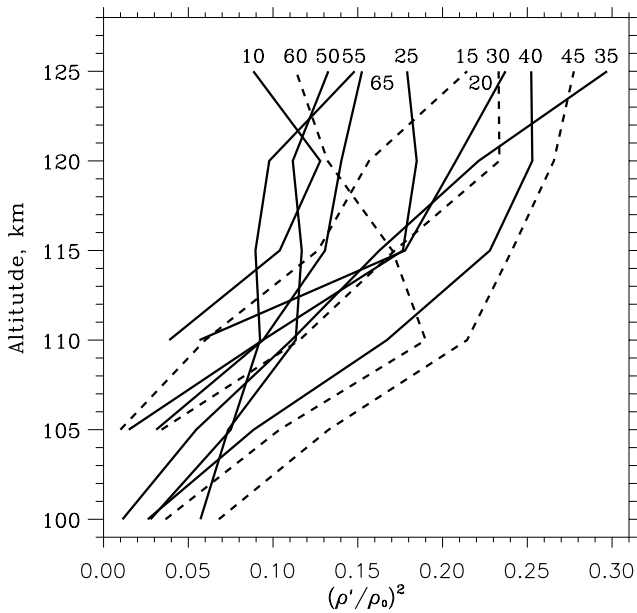


**Figure 13.** As in Figure 12, but showing vertical profiles of 5-day mean density ratio variances. Note the very different vertical profiles suggesting greater filtering of the GW field at earlier and later times.

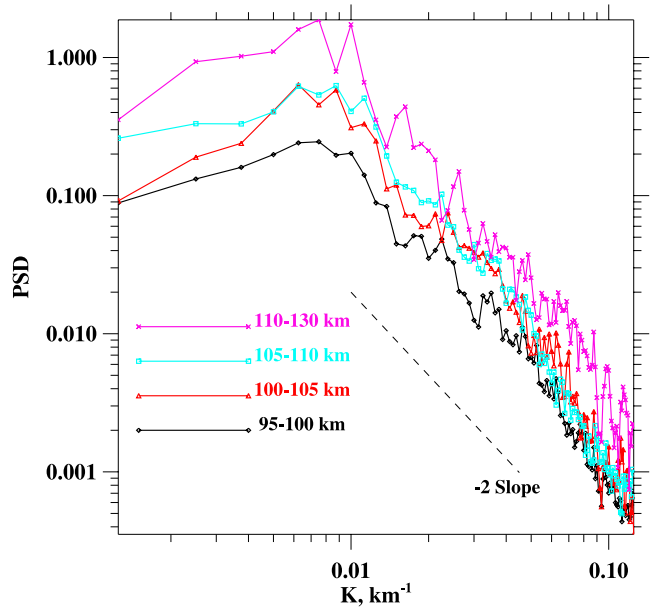


**Figure 14.** Horizontal wave number spectra computed from 200 1-s fractional perturbation densities about periapsis and extending to the same altitude on either side in order to compute spectra at approximately a constant altitude. The four spectra are for periapsis altitudes between 95 and 100 km (52 orbits, black), 100 and 105 km (28 orbits, red), 105 and 110 km (33 orbits, blue), and 110 and 130 km (12 orbits, magenta). The spatial scales were based on the true speed of the ODY spacecraft (with a mean of  $\sim 4$  km/sec), yielding a Nyquist wave number of 8 km. Note that there is no apparent noise floor in these data. The dashed line shows a spectral slope of  $-2$  for reference.

on Earth, both at the surface and via shear instabilities, nonlinear interactions, and other possible sources at lower altitudes (though the smaller number of atmospheric scale heights spanning Mars’ lower and middle atmosphere relative to Earth would offset this effect to an unknown degree). Finally, Mars winter jet wind speeds are believed to be much larger than on Earth, allowing for both larger GW amplitudes and larger vertical scales than expected on Earth.

[26] Given the above, we expect that GWs on Mars may have dramatic effects on the large-scale circulation and thermal structure, as suggested in several studies cited in the introduction. The study by *Barnes* [1990], in particular, anticipated GW drag of  $\sim 1000 \text{ m s}^{-1} \text{ sol}^{-1}$  or larger at altitudes of  $\sim 50$ – $100$  km. In comparison, the GW momentum flux estimate above, when scaled to lower altitudes in a manner consistent with the observed growth in spectral amplitude seen in Figure 14 (a change in variance or momentum flux per unit mass of  $\sim 5$  across  $\sim 25$  km), yields a body force of

$$\begin{aligned} dU/dt &\sim (1/\rho_0)d(\rho_0\langle u'_h w' \rangle)/dz \sim \langle u'_h w' \rangle/2H \\ &\sim 1000 \text{ m s}^{-1} \text{ sol}^{-1} \end{aligned} \tag{4}$$

at  $\sim 70$ – $80$  km (where  $H$  is the density scale height), with values  $\sim 5$  times smaller and larger at 50 and 100 km (but obviously very uncertain), respectively, thus spanning the range anticipated by *Barnes* [1990]. Thus our estimates

appear to confirm earlier suggestions that GWs may be expected to play a much more significant role in defining atmospheric circulation, structure, and variability on Mars than on Earth, where their effects are already recognized to be substantial. As noted above, however, momentum fluxes for the large-amplitude GWs often observed in the lower thermosphere could easily be significantly larger, and suggest possibly larger values at lower altitudes as well.

[27] GW-driven residual circulations implied by these accelerations are  $\sim 70 \text{ m s}^{-1}$  at  $\sim 70\text{--}80 \text{ km}$  and  $\sim 5$  times smaller (larger) at  $\sim 50\text{--}(100\text{--}) \text{ km}$  altitudes and at high latitudes. Like the momentum fluxes estimated above, these induced meridional motions are substantially larger than their terrestrial analogs. Likewise, we expect stronger instability dynamics and turbulent mixing accompanying the larger GW amplitudes occurring at higher latitudes and altitudes in the winter hemisphere. It is unclear, however, how the (apparently opposing) effects of vertical mixing due to enhanced GW breaking and the vertical transport by the GW-induced residual circulation (expected to yield a mean downward motion in these regions) will influence the composition of Mars' upper atmosphere at high latitudes in the winter hemisphere.

## 5. Summary and Conclusions

[28] We have used MGS and ODY aerobraking density data to evaluate mean structures and ODY data to assess GW amplitudes, variances, and variance variations with latitude, longitude, and seasonal and shorter timescales. MGS data exhibited a significant density enhancement (by more than a factor of 2) relative to ODY mean densities between  $\sim 115$  and  $135 \text{ km}$  in Mars northern winter during the Noachis dust storm. We also observed very different mean density distributions with latitude under fall and winter northern hemisphere conditions.

[29] GW amplitudes and spatial scales were inferred from ODY 1-s density data, as MGS data at this temporal resolution were unavailable for this analysis, due to the broken solar array that induced  $\sim 7\text{-s}$  oscillations of the spacecraft. ODY data were available only during northern winter, but they nevertheless allowed us to explore the variability of GW variances with altitude, latitude, longitude, and time. Fractional density perturbations were inferred from the ratio of 1-s data to a 39-s running mean in order to remove biases due to rapid density variations with altitude. This yielded high sensitivity to smaller spatial scales, but insensitivity to scales larger than  $\sim 200 \text{ km}$ . Thus our statistics are appropriate only for the smaller scales of motions contained in the "high-pass" filter.

[30] Fractional density perturbations were much more reliable early in the ODY mission, given the 2x reductions in accelerometer samplings beginning on orbit  $\sim 135$  and again on orbit  $\sim 270$ . Distributions of GW variance with altitude and longitude suggest variance enhancements occurring in longitude bands centered near  $\sim 0\text{--}50^\circ$  and  $\sim 130\text{--}180^\circ$  that might be indicative of filtering by non-migrating tides and/or planetary waves. Because these data do not sample all longitudes and local times, however, it proved difficult to separate the spatial and temporal variability with complete confidence. Thus we also examined the temporal variability of these GW variances. This anal-

ysis suggested significant temporal variability having coherence in altitude and time, but again suggesting filtering by larger-scale motions imposing variable zonal winds, wind shears, and/or density variations.

[31] Finally, we computed horizontal wave number spectra of fractional density perturbations and examined their variations with altitude. These revealed a consistent spectral shape with increasing altitude and a spectral amplitude growth much smaller than that expected in the absence of GW instability and dissipation processes. This was interpreted as evidence of a saturated GW spectrum, suggesting vigorous instability processes, local body forcing, and a potential to estimate GW parameters and momentum fluxes based on saturation theory.

[32] Estimates of GW momentum fluxes resulting from the large observed fractional density fluctuations, the relatively small horizontal scales, and the inferred large vertical scales and vertical velocities yielded values dramatically larger than observed at comparable altitudes and atmospheric densities on Earth. These suggest that GWs in the Mars atmosphere may have substantially larger influences on the larger-scale mean, tidal, and planetary-wave motions, on constituent transports, and on overall atmospheric variability than on Earth.

[33] **Acknowledgments.** This research was supported by the NASA Mars Data Analysis Program through NASA contract NNN06CC06C.

[34] Amitava Bhattacharjee thanks Jeff Barnes and Stephen Bougher for their assistance in evaluating this paper.

## References

- Angelats i Coll, M., F. Forget, M. A. López-Valverde, and F. González-Galindo (2005), The first Mars thermospheric general circulation model: The Mars atmosphere from the ground to  $240 \text{ km}$ , *Geophys. Res. Lett.*, *32*, L04201, doi:10.1029/2004GL021368.
- Banfield, D., A. Ingersoll, and C. Keppenne (1995), A steady-state Kalman filter for assimilating data from a single polar-orbiting satellite, *J. Atmos. Sci.*, *52*, 737–753.
- Banfield, D., B. J. Conrath, J. C. Pearl, M. D. Smith, and P. R. Christensen (2000), Thermal tides and stationary waves on Mars as revealed by Mars Global Surveyor Thermal Emission Spectrometer, *J. Geophys. Res.*, *105*, 9521–9537.
- Banfield, D., B. J. Conrath, M. D. Smith, P. R. Christensen, and R. J. Wilson (2003), Forced waves in the Mars atmosphere from MGS TES Nadir data, *Icarus*, *161*, 319–345.
- Banfield, D., B. J. Conrath, P. J. Gierasch, R. J. Wilson, and M. D. Smith (2004), Traveling waves in the martian atmosphere from MGS TES Nadir data, *Icarus*, *170*, 365–403.
- Barnes, J. R. (1990), Possible effects of breaking gravity waves on the circulation of the middle atmosphere of Mars, *J. Geophys. Res.*, *95*, 1401–1421.
- Blamont, J. E., and E. Chassefiere (1993), First detection of ozone in the middle atmosphere of Mars from solar occultation measurements, *Icarus*, *104*, 324–336.
- Bougher, S. W., J. M. Bell, J. R. Murphy, M. A. Lopez-Valverde, and P. G. Withers (2006a), Polar warming in the Mars thermosphere: Seasonal variations owing to changing insolation and dust distributions, *Geophys. Res. Lett.*, *33*, L02203, doi:10.1029/2005GL024059.
- Bougher, S. W., J. R. Murphy, J. M. Bell, and R. W. Zurek (2006b), Predictions of the structure of the martian atmosphere for the Mars Reconnaissance Orbiter (MRO) mission, *Mars*, *2*, 10–20, doi:10.1555/mars.2006.002.
- Briggs, G., and C. B. Leovy (1974), Mariner 9 observations of the Mars north polar hood, *Bull. Am. Meteorol. Soc.*, *55*, 278–296.
- Briggs, G. A., W. A. Baum, and J. R. Barns (1979), Viking Orbiter imaging observations of dust in the Mars atmosphere, *J. Geophys. Res.*, *84*, 2795–2820.
- Collins, M., S. R. Lewis, and P. L. Read (1997), Gravity wave drag in a global circulation model of the Mars atmosphere: Parameterization and validation, *Adv. Space Res.*, *19*, 1245–1254.
- Creasey, J. E., J. M. Forbes, and D. P. Hinson (2006), Global and seasonal distributions of gravity wave activity in Mars' lower atmosphere derived

- from MGS radio occultation data, *Geophys. Res. Lett.*, *33*, L01803, doi:10.1029/2005GL024037.
- Deming, D., M. J. Mumma, F. Espenak, T. Kostiuik, and D. Zipoy (1986), Polar warming in the atmosphere of Mars, *Icarus*, *66*, 366–379.
- Eckermann, S. D., and C. J. Marks (1997), GROGRAT: A new model of the global propagation and dissipation of atmospheric gravity waves, *Adv. Space Res.*, *20*(6), 1253–1256.
- Forbes, J. M., and M. E. Hagan (2000), Diurnal Kelvin wave in the atmosphere of Mars: Towards an understanding of “stationary” density structures observed by the MGS accelerometer, *Geophys. Res. Lett.*, *27*, 3563–3566.
- Forget, F., F. Hourdin, R. Fournier, C. Hourdin, O. Talagrand, M. Collins, S. R. Lewis, P. L. Read, and J.-P. Huot (1999), Improved general circulation models of the Mars atmosphere from the surface to above 80 km, *J. Geophys. Res.*, *104*(24), 155–175.
- Fritts, D. C., and M. J. Alexander (2003), Gravity dynamics and effects in the middle atmosphere, *Rev. Geophys.*, *41*(1), 1003, doi:10.1029/2001RG000106.
- Fritts, D. C., S. A. Smith, B. B. Balsley, and C. R. Philbrick (1988), Evidence of gravity wave saturation and local turbulence production in the summer mesosphere and lower thermosphere during the STATE experiment, *J. Geophys. Res.*, *93*, 7015–7025.
- Fritts, D. C., R. C. Blanchard, and L. Coy (1989), Gravity wave structure between 60 and 90 km inferred from space shuttle reentry data, *J. Atmos. Sci.*, *46*, 423–434.
- Fritts, D. C., D.-Y. Wang, and R. C. Blanchard (1993), Gravity wave and tidal structures between 60 and 140 km inferred from space shuttle re-entry data, *J. Atmos. Sci.*, *50*, 785–806.
- Fritts, D. C., S. A. Vadas, and Y. Yamada (2002), An estimate of strong local gravity wave body forcing based on OH airglow and meteor radar observations, *Geophys. Res. Lett.*, *29*(10), 1429, doi:10.1029/2001GL013753.
- Guest, F. M., M. J. Reeder, C. J. Marks, and D. J. Karoly (2000), Inertia-gravity waves observed in the lower stratosphere over Macquarie Island, *J. Atmos. Sci.*, *57*, 737–752.
- Hertzog, A., F. Vial, A. Dörnbrack, S. D. Eckermann, B. M. Knudsen, and J.-P. Pommereau (2002), In-situ observations of gravity waves and comparisons with numerical simulations during the SOLVE/THESEO 2000 campaign, *J. Geophys. Res.*, *107*(D20), 8292, doi:10.1029/2001JD001025.
- Hinson, D. P., R. A. Simpson, J. D. Twicken, G. L. Tyler, and F. M. Flasar (1999), Initial results from radio occultation measurements with Mars Global Surveyor, *J. Geophys. Res.*, *104*, 26,997–27,012.
- Houben, H. (1999), Assimilation of Mars Global Surveyor meteorological data, *Adv. Space Res.*, *23*(11), 1899–1902.
- Jasperson, W. H., G. D. Nastrom, and D. C. Fritts (1990), Further study of terrain effects on the mesoscale spectrum of atmospheric motions, *J. Atmos. Sci.*, *47*, 979–987.
- Jiang, J. H., D. L. Wu, and S. D. Eckermann (2002), Upper Atmosphere Research Satellite (UARS) MLS observation of mountain waves over the Andes, *J. Geophys. Res.*, *107*(D20), 8273, doi:10.1029/2002JD002091.
- Jiang, J. H., D. L. Wu, S. D. Eckermann, and J. Ma (2003), Mtn. waves in the middle atmosphere: Microwave Limb Sounder observations and analyses, *Adv. Space Res.*, *32*(5), 801–806.
- Jiang, J. H., S. D. Eckermann, D. L. Wu, and J. Ma (2004), A search for mountain waves in MLS stratospheric limb radiance from the Northern Hemisphere: Data analysis and global mountain wave modeling, *J. Geophys. Res.*, *109*, D03107, doi:10.1029/2003JD003974.
- Joshi, M. M., B. N. Lawrence, and S. R. Lewis (1995), Gravity wave drag in three-dimensional atmospheric models of Mars, *J. Geophys. Res.*, *100*, 21,235–21,245.
- Joshi, M. M., B. N. Lawrence, and S. R. Lewis (1996), The effect of spatial variations in unresolved topography on gravity wave drag in the Martian atmosphere, *Geophys. Res. Lett.*, *23*, 2927–2930.
- Joshi, M. M., J. A. Magalhães, and S. D. Eckermann (1999), Investigating the propagation of gravity waves in the Mars atmosphere using a ray-tracing model, in *Geophysical Research Abstracts: 24th General Assembly of the European Geophysical Society*, p. PS4.4, Eur. Geophys. Soc., Abeystwyth, UK.
- Keating, G., et al. (1998), The structure of the upper atmosphere of Mars: In situ accelerometer measurements from Mars Global Surveyor, *Science*, *279*, 1672–1676.
- Keating, G. M., et al. (2001), Persistent planetary-scale wave-2 and wave-3 density variations observed in Mars upper atmosphere from MGS accelerometer experiment, *Proc. Eur. Geophys. Soc.*, *78*, 229.
- Keating, G. M., R. H. Tolson, M. E. Theriot, J. L. Hanna, A. M. Dwyer, S. W. Bougher, and R. W. Zurek (2002), Detection of winter polar warming in Mars upper atmosphere, *Proc. Eur. Geophys. Soc.*, *79*, 266.
- Lewis, S. R., and P. L. Read (1995), An operational data assimilation scheme for the Martian atmosphere, *Adv. Space Res.*, *16*(6), 9–13.
- Lewis, S. R., M. Collins, and P. L. Read (1996), Martian atmospheric data assimilation with a simplified general circulation model: Orbiter and lander networks, *Planet. Space Sci.*, *44*, 1395–1409.
- Lewis, S. R., M. Collins, and P. L. Read (1997), Data assimilation with a Martian atmospheric GCM: An example using thermal data, *Adv. Space Res.*, *19*(8), 1267–1270.
- Magalhães, J. A., J. T. Schofield, and A. Seiff (1999), Results of the Mars Pathfinder atmospheric structure investigation, *J. Geophys. Res.*, *104*(E4), 8943–8956.
- Marks, C. J., and S. D. Eckermann (1995), A three-dimensional nonhydrostatic ray-tracing model for gravity waves: Formulation and preliminary results for the middle atmosphere, *J. Atmos. Sci.*, *52*, 1959–1984.
- Nastrom, G. D., and D. C. Fritts (1992), Sources of mesoscale variability of gravity waves, I: Topographic excitation, *J. Atmos. Sci.*, *49*, 101–110.
- Pettengill, G. H., and P. G. Ford (2000), Winter clouds over the north Martian polar cap, *Geophys. Res. Lett.*, *27*, 609–612.
- Pirraglia, J. A. (1976), Martian atmospheric lee waves, *Icarus*, *27*, 517–530.
- Preusse, P., A. Dörnbrack, S. D. Eckermann, M. Riese, B. Schaeler, J. T. Bacmeister, D. Broutman, and K. U. Grossmann (2002), Space-based measurements of stratospheric mountain waves by CRISTA: 1. Sensitivity, analysis method, and a case study, *J. Geophys. Res.*, *107*(D23), 8178, doi:10.1029/2001JD000699.
- Rafkin, S. C. R., R. Haberle, and T. I. Michaels (2001), The Mars regional atmospheric modeling system: Model description and selected simulations, *Icarus*, *151*, 228–256.
- Read, P. L., and S. R. Lewis (2004), *The Martian Climate Revisited*, 326 pp., Springer, New York.
- Sentman, D. D., E. M. Wescott, R. H. Picard, J. R. Winick, H. C. Stenbaek-Nielsen, E. M. Dewan, D. R. Moudry, F. T. Sao Sabbas, and M. J. Heavner (2003), Simultaneous observation of mesospheric gravity waves and sprites generated by a Midwestern thunderstorm, *J. Atmos. Sol. Terr. Phys.*, *65*, 537–550.
- Taylor, M. J., and M. A. Hapgood (1988), Identification of a thunderstorm as a source of short period gravity waves in the upper atmosphere night-glow emissions, *Planet. Space Sci.*, *36*, 975.
- Theodore, B., E. Lellouch, E. Chassefiere, and A. Hauchecorne (1993), Solstitial temperature inversions in the Martian middle atmosphere: Observational clues and 2-D modeling, *Icarus*, *105*, 512–528.
- Tolson, R. H., et al. (1999), Application of accelerometer data to Mars Global Surveyor aerobraking operations, *J. Spacecr. Rockets*, *36*(3), 323–329.
- Tolson, R. H., et al. (2000), Utilization of Mars Global Surveyor accelerometer data for atmospheric modeling, *Astrodynamic 1999, Adv. Astronaut. Sci.*, *103*, 1329–1346.
- Tolson, R. H., et al. (2002), Application of accelerometer data to Mars Odyssey aerobraking and atmospheric modeling, *J. Spacecr. Rockets*, *42*, 435–443.
- Vadas, S. L., and D. C. Fritts (2004), Thermospheric responses to gravity waves arising from mesoscale convective complexes, *J. Atmos. Solar Terr. Phys.*, *66*, 781–804.
- Vadas, S. L., and D. C. Fritts (2005), Thermospheric responses to gravity waves: Influences of increasing viscosity and thermal diffusivity, *J. Geophys. Res.*, *110*, D15103, doi:10.1029/2004JD005574.
- Vadas, S. L., and D. C. Fritts (2006), The influence of increasing temperature and solar variability on gravity wave structure and dissipation in the thermosphere, *J. Geophys. Res.*, *111*, A10S12, doi:10.1029/2005JA011510.
- Wang, L., D. C. Fritts, and R. H. Tolson (2006), Nonmigrating tides inferred from the Mars Odyssey and Mars Global Surveyor aerobraking data, *Geophys. Res. Lett.*, doi:10.1029/2006GL027753, in press.
- Wilson, R. J. (2002), Evidence for nonmigrating thermal tides in the Mars upper atmosphere from the Mars Global Surveyor Accelerometer Experiment, *Geophys. Res. Lett.*, *29*(7), 1120, doi:10.1029/2001GL013975.
- Wilson, R. J., and K. Hamilton (1996), Comprehensive model simulation of thermal tides in the Martian Atmosphere, *J. Atmos. Sci.*, *53*, 1290–1326.
- Withers, P. (2006), Mars Global Surveyor and Mars Odyssey Accelerometer observations of the Martian upper atmosphere during aerobraking, *Geophys. Res. Lett.*, *33*, L02201, doi:10.1029/2005GL024447.
- Yamada, Y., H. Fukunishi, T. Nakamura, and T. Tsuda (2001), Breakdown of small-scale quasi-stationary gravity wave and transition to turbulence observed in OH airglow, *Geophys. Res. Lett.*, *28*, 2153–2156.
- Zhang, K. Q., A. P. Ingersoll, D. M. Kass, J. C. Pearl, M. D. Smith, and B. J. Conrath (2001), Assimilation of Mars Global Surveyor atmospheric temperature data into a general circulation model, *J. Geophys. Res.*, *106*(E12), 32,863–32,877.

D. C. Fritts and L. Wang, Colorado Research Associates Division, NorthWest Research Associates, 3380 Mitchell Lane, Boulder, CO 80301, USA. (dave@cora.nwra.com)